

Rapid Depolarization-Free Nanoscopic Background Elimination of Cellular Metallic Nanoprobes

Yunbo Liu, Di Zu, Zhijia Zhang, Xintao Zhao, Guangjie Cui, Mario Hentschel, Younggeun Park, and Somin Eunice Lee*

The crowded intracellular environment of biomolecules, including organelles, solutes, proteins, and membranes, presents distinct biomolecular dynamics crucial for the functions of biomolecules within living cells. However, background suppression is critical to uncover nanoscale dynamics in living cells. Herein, a new method for enabling rapid, nanoscale background elimination of cellular metallic nanoprobes is presented. By employing integrated nanoscopic correction (iNC) designed to eliminate depolarization effects, which compromise background elimination, a real-time algorithm to subtract and increment orthogonal pairs of polarizations for real-time nanoscale background elimination is introduced. The ability to analyze orthogonal pairs at high speed over the entire polarization range is currently difficult to achieve using conventional methods. By processing orthogonal pairs in real time, this method minimizes movement artifacts during the background elimination process. Nanometer spatial stability which enables two orders of magnitude increase in signal-to-noise ratio of cellular metallic nanoprobes is shown. Nanoscale background elimination aiding the ability to accurately track biomolecules and their dynamics in living cells is anticipated.

1. Introduction

Within living cells, the intracellular space is crowded with biomolecular constituents, including organelles, solutes, proteins, and membranes. Such crowded and heterogeneous distributions present distinct dynamics crucial for the functions of biomolecules within living cells.^[1] Biomolecules within the intracellular space are routinely studied using fluorescent probes. Recently, fluorescence super-resolution^[2–8] offers nanoscale spatial resolution of fluorescently labeled biomolecules. However, the reliance on fluorescence has shortcomings for imaging dynamics. In the excited state, fluorophores can undergo permanent structural changes, resulting in permanent photobleaching and, thus, limiting the ability to track biomolecules and their dynamics in the intracellular space.


Attractive alternatives to fluorophores are plasmonic nanoprobes.^[9–29] Unlike fluorophores, plasmonic nanoprobes undergo elastic scattering, and, therefore, do not photobleach or blink. The collective oscillation of electrons of plasmonic nanoprobes gives rise to strong interactions with photons, inducing extraordinarily large scattering cross sections as biomolecular recognition probes in super-resolution imaging. However, as organelles, proteins, and membranes crowding the intracellular space also undergo elastic scattering, background scattering presents a significant challenge for the use of plasmonic scatterers as probes of biomolecular dynamics in the intracellular space.

To suppress background scattering, cross-polarization^[30–32] has been highly effective at providing high-contrast imaging of plasmonic nanoprobes. In cross-polarization, a polarizer is placed in the illumination path creating linearly polarized illumination, followed by the sample specimen labeled with anisotropic plasmonic nanoprobes, and subsequently followed by another polarizer placed in the detection path aligned orthogonally with respect to the other polarizer. In principle, any depolarization of the polarized electric field is solely by anisotropic plasmonic nanoprobes. Intracellular biomolecules are considered to be isotropic and, therefore, do not contribute to depolarization. However, high numerical aperture condensers in the illumination path have been found to induce undesirable depolarization effects,^[33] a partial conversion of the polarized electric field to arbitrary polarizations at the focus, contributing to the

Y. Liu, D. Zu, Z. Zhang, X. Zhao, G. Cui, S. E. Lee
Department of Electrical & Computer Engineering, Biomedical
Engineering, Applied Physics, Biointerfaces Institute, Macromolecular
Science & Engineering
University of Michigan
Ann Arbor, MI 48109-2122, USA
E-mail: sleee@umich.edu

M. Hentschel
4th Physics Institute and Research Center SCoPE
University of Stuttgart
Stuttgart 70569, Germany

Y. Park
Department of Mechanical Engineering
University of Michigan
Ann Arbor, MI 48109-2122, USA

 The ORCID identification number(s) for the author(s) of this article can be found under <https://doi.org/10.1002/aisy.202200180>.

© 2022 The Authors. Advanced Intelligent Systems published by Wiley-VCH GmbH. This is an open access article under the terms of the Creative Commons Attribution License, which permits use, distribution and reproduction in any medium, provided the original work is properly cited.

DOI: 10.1002/aisy.202200180

background. The signal-to-noise ratio (SNR) with depolarization effects can be written as

$$\text{SNR}_d = \frac{\sum_{\theta} |I_s + A(\theta)|}{\sum_{\theta} |B(\theta) + \text{Noise}|} \quad (1)$$

summed over the polarization range where I_s is the intensity of the signal, and A and B are intensity contributions from depolarization effects where $A \neq B$ and noise is photon shot noise. When images at orthogonal polarizations are acquired, Equation (1) shows depolarization effects that are unable to be subtracted out due to being at different arbitrary polarizations. Furthermore, mechanical means to rotate the polarization during image acquisition introduce spatial errors, which also are unable to be subtracted out, further impeding background suppression as well as imposing time constraints on the background suppression process.

In this work, we introduce a new method for enabling nanoscale background elimination of intracellular metallic nanoprobe. We employ integrated nanoscopic correction (iNC) designed to eliminate depolarization effects. Here, the iNC is placed in the detection path between the objective and the tube lens (Figure 1). Because the region between the objective and the tube lens provides a path of parallel light rays, when images at orthogonal polarizations are acquired by the iNC, background subtraction free from depolarization effects is feasible. Then, the SNR free from depolarization effects can be written as

$$\text{SNR} = \frac{\sum_{\theta} |I_{s\parallel} - I_{s\perp}|}{\sum_{\theta} |I_{bg\parallel} - I_{bg\perp}|} = \frac{\sum_{\theta} |I_s|}{\sum_{\theta} |\text{Noise}|} \quad (2)$$

summed over the polarization range where $I_{s\parallel}$ and $I_{s\perp}$ are the intensities of the signal orthogonal pair, and $I_{bg\parallel}$ and $I_{bg\perp}$ are the intensities of the background orthogonal pair. Since intracellular constituents contributing to the background are considered to be isotropic, $I_{bg\parallel}$ and $I_{bg\perp}$ will be approximately similar. With $I_{s\parallel}$ and $I_{s\perp}$ primarily contributing to the SNR, the SNR is enhanced in the final background-free image. We introduce a real-time algorithm to subtract and increment orthogonal pairs of polarizations for real-time nanoscale background elimination. We show that nanometer spatial stability substantially increases SNR of intracellular metallic nanoprobe by two orders of magnitude. We expect that nanoscale background elimination will facilitate precise tracking of biomolecules and their dynamics in living cells.

2. Results and Discussion

For real-time background elimination, we employed the iNC^[14] consisting of liquid crystal and fixed retarders in the detection path of a transmission mode dark-field microscope (Figure 1b). The iNC was modulated by voltage between 3 and 14 V (Figure S1, Supporting Information) with millisecond high speed (Figure S2, Supporting Information) such that the change

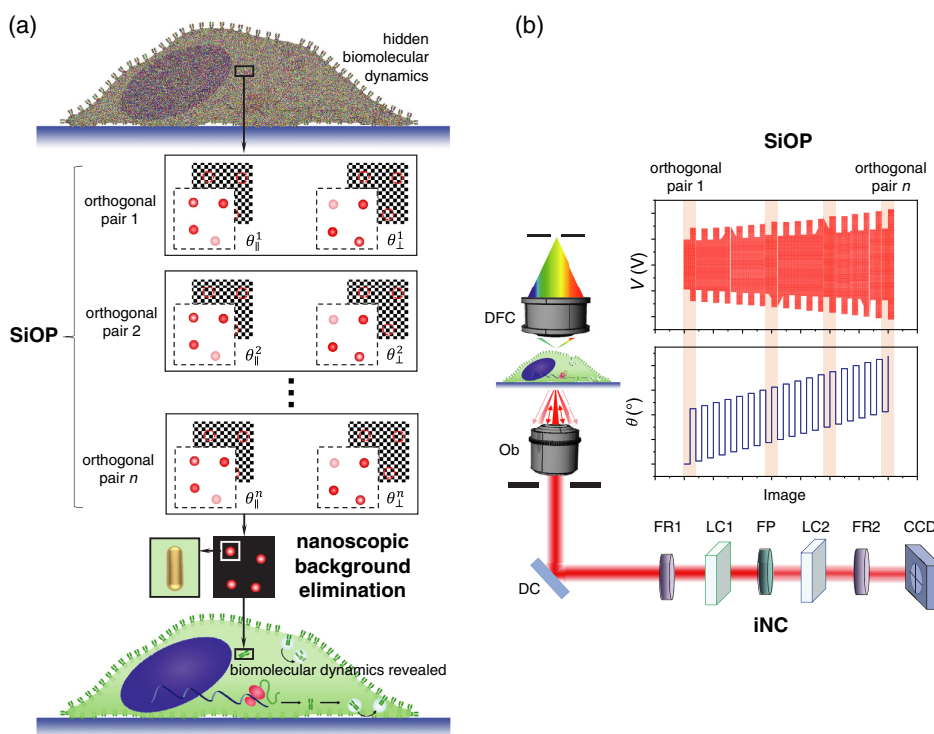


Figure 1. Nanoscopic background elimination of cellular metallic nanoprobe. a) Conceptual schematic of hidden biomolecular dynamics due to background scattering. SiOP enables nanoscale background elimination in living cells. SiOP subtracts and increments orthogonal pairs θ_{\parallel} , θ_{\perp} in real time to study biomolecular dynamics in living cells. b) Conceptual schematic of experimental setup: iNC was integrated into a transmission dark-field microscope. DFC, dark-field condenser; Ob, objective; DC, dichroic mirror; FR1, fixed retarder; LC1, liquid crystal retarder; FP, fixed polarizer; LC2, liquid crystal retarder; FR2, fixed retarder; CCD, charge-coupled detector. SiOP algorithm controls voltage to the iNC to subtract and increment orthogonal pairs θ_{\parallel} , θ_{\perp} .

in output transmission intensity corresponds to different input polarizations. To implement real-time background elimination, we developed the subtract increment orthogonal pair (SiOP) algorithm to control voltage to the iNC to subtract and increment orthogonal pairs of polarizations (Figure 2). To process the polarization range from 0° to 180°, the voltage train of SiOP consisted of θ_{\parallel} ranging from 0° to 90° and θ_{\perp} ranging from 90° to 180° in increments of α . SiOP was acquired and subtracted images for each orthogonal pair over the entire polarization range (Figure 2a, S3, Supporting Information). By processing orthogonal pairs in real time, this method minimizes the potential for movement artifacts during the background elimination process. The ability to process orthogonal pairs at high speed over the entire polarization range is made possible by the iNC and is currently difficult to achieve using conventional methods.

To demonstrate the principle of SiOP, we first calculated the electric field norm distribution for various orthogonal pairs at wavelength $\lambda = 740$ nm (Figure 2c), supporting that orthogonality

can be maintained as orthogonal pairs are incremented over the entire polarization range. We observed similar orthogonality using other geometries (Figure S4, Supporting Information), demonstrating the universality of our method. To validate SiOP, we lithographically patterned individual gold nanorods (AuNRs) of known orientations (0°, 30°, 60°, and 90° with respect to the x -axis) with dimensions 44 nm \times 125 nm by electron beam lithography (Figure S5, Supporting Information, Figure 2d). As AuNRs exhibit collective oscillation of electrons along their longitudinal axis, unpolarized illumination was scattered at selective polarizations. Unpolarized illumination was unselectively scattered by background constituents. At the start of the voltage train (Figure 2a,i), SiOP acquired and subtracted dark-field images for orthogonal pair of polarizations θ_{\parallel} , θ_{\perp} (0°, 90°), as shown in Figure 2d,i, resulting in the subtracted image I_{sub} . As shown in Figure 2d,i, the AuNRs oriented at 0° with respect to the x -axis showed the maximum intensity for the orthogonal pair of polarizations θ_{\parallel} , θ_{\perp} (0°, 90°). In the middle of the voltage train

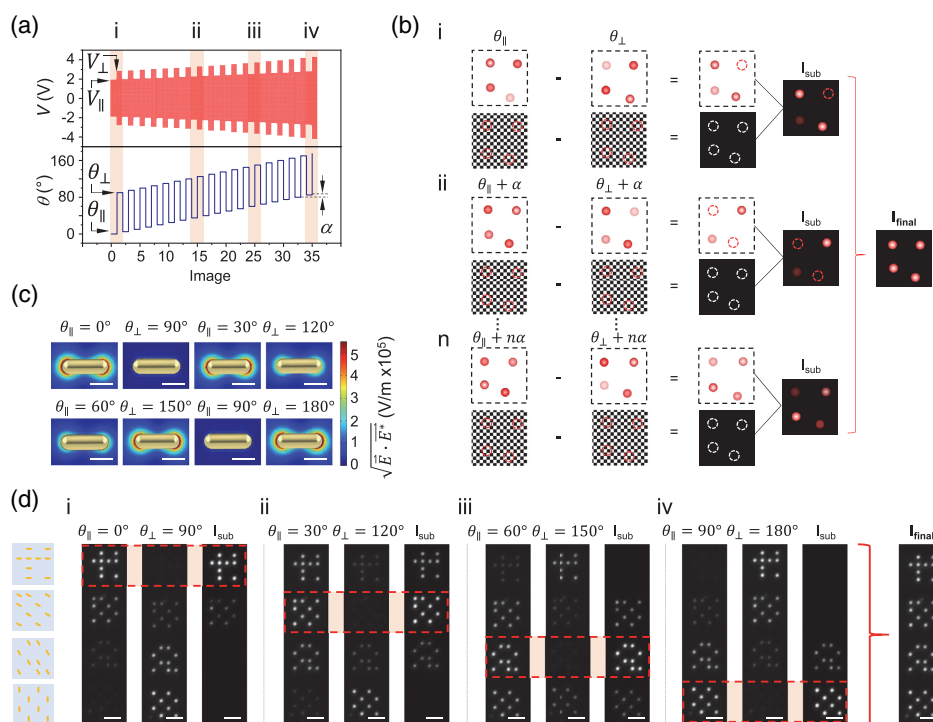


Figure 2. Subtract increment orthogonal pair (SiOP) algorithm enables real-time nanoscale background elimination. a) SiOP algorithm controls voltage to the iNC to subtract and increment orthogonal pairs θ_{\parallel} , θ_{\perp} . (top) Graph of input voltage V versus image number. (bottom) Graph of transmission polarization θ versus image number. Orthogonal pair $(\theta_{\parallel}, \theta_{\perp})$: V_{\parallel} corresponds to θ_{\parallel} and V_{\perp} corresponds to θ_{\perp} . α : increment. i–iv: input V and transmission polarization θ corresponding to part d. b) Conceptual schematic of SiOP algorithm to subtract and increment orthogonal pairs: red circles represent arbitrarily oriented plasmonic nanoprobe. i) SiOP subtracts images of orthogonal pair $(\theta_{\parallel}, \theta_{\perp})$. ii) SiOP increments by α to the next orthogonal pair and subtracts. n) SiOP continues to increment by α over the polarization range from 0° to 180°. Finally, SiOP sums images I_{sub} to obtain the final background-free image I_{final} . c) Calculated electric field norm $\sqrt{E \cdot E^*}$ distribution for orthogonal pairs θ_{\parallel} , θ_{\perp} (0°, 90°), (30°, 120°), (60°, 150°), and (90°, 180°). Scale bar: 50 nm. d) Conceptual schematic of nanorods of known orientations at 0°, 30°, 60°, and 90° with respect to the x -axis. i) Experimental dark-field images of orthogonal pair θ_{\parallel} , θ_{\perp} (0°, 90°) corresponding to part a i acquired and subtracted by SiOP. I_{sub} : subtracted image of orthogonal pair. ii) Experimental dark-field images of orthogonal pair θ_{\parallel} , θ_{\perp} (30°, 120°) corresponding to part a ii acquired and subtracted by SiOP. I_{sub} : subtracted image of orthogonal pair. iii) Experimental dark-field images of orthogonal pair θ_{\parallel} , θ_{\perp} (60°, 150°) corresponding to part a iii acquired and subtracted by SiOP. I_{sub} : subtracted image of orthogonal pair. iv) Experimental dark-field images of orthogonal pair θ_{\parallel} , θ_{\perp} (90°, 180°) corresponding to part a iv acquired and subtracted by SiOP. I_{sub} : subtracted image of orthogonal pair. Finally, SiOP sums images I_{sub} over the entire polarization range to obtain the final background-free image I_{final} . Scale bar: 5 μm .

(Figure 2a,ii), SiOP then subtracted dark-field images for orthogonal pair of polarizations $\theta_{\parallel}, \theta_{\perp}$ ($30^{\circ}, 120^{\circ}$), as shown in Figure 2d, ii. In the subtracted image I_{sub} (Figure 2d,ii), the AuNRs oriented at 30° displayed the highest intensity for the orthogonal pair $\theta_{\parallel}, \theta_{\perp}$ ($30^{\circ}, 120^{\circ}$). Likewise, for the orthogonal pair $\theta_{\parallel}, \theta_{\perp}$ ($60^{\circ}, 150^{\circ}$), as shown in Figure 2a,iii,d,iii, the AuNRs oriented at 60° showed the highest intensity. At the end of the voltage train, as shown in Figure 2a,iv,d,iv, the AuNRs oriented at 90° displayed the maximum intensity for the orthogonal pair $\theta_{\parallel}, \theta_{\perp}$ ($90^{\circ}, 180^{\circ}$). Finally, SiOP summed images I_{sub} to obtain the final background-free image I_{final} . SiOP eliminated background artifacts (Figure S6, Supporting Information). Since background artifacts are considered to be isotropic, the orthogonal pair was approximately similar to the background artifact, as shown in Figure S6, Supporting Information, while the AuNRs were distinctly different in the orthogonal pair. After SiOP, the background artifact was eliminated.

We next applied SiOP to address spatial errors in background suppression. In Equation (1) and (2), the assumption is there are no spatial shifts in I_s . However, if spatial shifts are present (Figure 3), then low SNR and distortion can significantly deteriorate background suppression (Figure 3a). To systematically study the impact of spatial errors on background suppression, we investigated lithographically patterned individual AuNRs of known orientation. When a mechanically rotated polarizer was used to rotate the polarization, spatial shifts arose due to the

rotating optics. As shown in Figure 3b, an individual AuNR oriented at 90° with respect to the x -axis was imaged at $\theta_1 = 70^{\circ}$ and $\theta_2 = 110^{\circ}$ by a mechanically rotated polarizer. At the different polarizations, the center position of the AuNR visibly shifted in position in the dark-field images, as shown in Figure 3b,i. To quantify the position shift, we analyzed 16 replicates and repeated 10 times the alternation between $\theta_1 = 70^{\circ}$ and $\theta_2 = 110^{\circ}$ for each replicate to measure the spatial shift. For the mechanically rotated polarizer, the mean spatial shift l was 61.4 nm with a standard deviation of 23 nm (Figure 3b,ii). This spatial shift negatively impacted background suppression. We observed visible distortion (Figure 3c,i) and low SNR (Figure 3c,ii). We calculated the root mean squared error ϵ between the intensities at each pixel and measured high ϵ as a result of the spatial shift (Figure 3c,iii). In contrast, SiOP with the iNC utilizes voltage control to modulate the transmission polarization. When the individual AuNR oriented at 90° was imaged at $\theta_1 = 70^{\circ}$ and $\theta_2 = 110^{\circ}$, the center position remained the same at different polarizations (Figure 3b,i). The mean spatial shift l was 7.1 nm with a 3.3 nm standard deviation (Figure 3b,ii). As compared to the mechanical polarizer, the iNC showed a significantly lower mean value and smaller standard deviation, indicating a lower spatial shift and higher repeatability. To further quantify the spatial shift, we measured the Pearson coefficient r as a quantitative metric for image similarity (Figure 3b,iii). The iNC showed a high r as compared to the

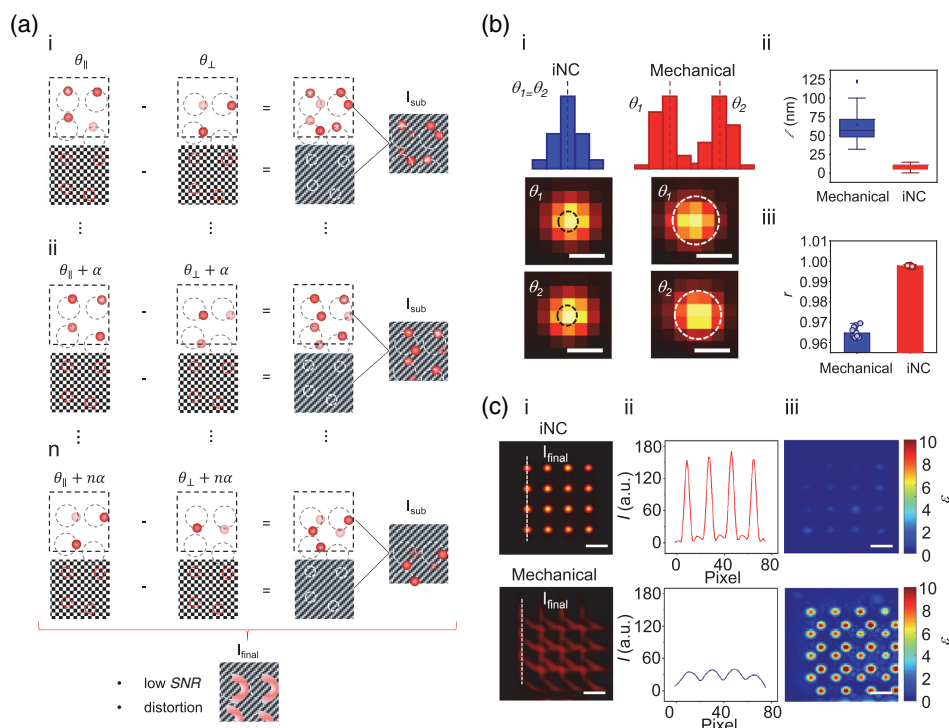


Figure 3. Nanometer spatial stability of iNC facilitates high signal-to-noise in nanoscale background elimination. a) Conceptual schematic of spatial errors arising from mechanically rotated polarizer. Spatial errors compromise background suppression. i–n: subtracted images illustrate spatial errors over the polarization range. b) i) Conceptual schematic of line profile of airy pattern for iNC versus mechanically rotated polarizer. Experimental dark-field images for $\theta_1 = 70^{\circ}$ and $\theta_2 = 110^{\circ}$ for iNC and mechanically rotated polarizer. ii) Graph of spatial shift l for iNC versus mechanically rotated polarizer. iii) Graph of Pearson coefficient r for iNC versus mechanically rotated polarizer. (c) i) Final images I_{final} for iNC versus mechanically rotated polarizer. ii) Graph of intensity line profile for iNC versus mechanically rotated polarizer. iii) Graph of RMS error ϵ for iNC versus mechanically rotated polarizer. Scale bar: 2.5 μm .

mechanical polarizer, indicating that images obtained using the iNC under different polarizations have high similarity. Thus, we were able to achieve a background-free image (Figure 3c,i) with high SNR (Figure 3c,ii). By processing orthogonal pairs in real time, our method has the potential to minimize other spatial errors, such as drifting and movement artifacts, during the background suppression process.

Having validated SiOP, we then proceeded to apply SiOP to cellular imaging (Figure 4). As a cellular model, we chose SH-SY5Y neuroblastoma cells. Under dark-field illumination, unpolarized illumination was unselectively scattered by cellular constituents and cellular constituents exhibited strong background scattering (Figure 4b,i). When SiOP was applied, background scattering was eliminated. To visualize nanoprobe, we synthesized biocompatible CTA+ free AuNRs (Bio-AuNRs) by bromide-free seed-mediated growth followed by ligand exchange.^[13] We incubated SH-SY5Y cells with Bio-AuNRs. Under dark-field illumination, unpolarized illumination was scattered at selective

polarizations by Bio-AuNRs (Figure 4b,ii). In region of interest I (Figure 4c), an individual nanoprobe was difficult to resolve due to background scattering. To eliminate background scattering, we applied SiOP. The voltage train of SiOP covered the polarization range from 0° to 180° (Figure 2a). SiOP acquired and subtracted dark-field images for orthogonal pair of polarizations over the polarization range. As SiOP incremented through the orthogonal pairs, we observed the individual nanoprobe modulate between bright and dark states. SiOP summed images I_{sub} to obtain the final background-free image I_{final} , revealing the individual nanoprobe, which could not be observed previously due to background scattering. In addition to individual nanoprobe, multiple nanoprobe were also difficult to resolve due to background scattering in region of interest II (Figure 4c). As nanoprobe were randomly distributed, we observed different nanoprobe modulate between bright and dark states according to different orthogonal pairs. After SiOP summed images I_{sub} to obtain the final background-free image I_{final} , we were able to resolve multiple

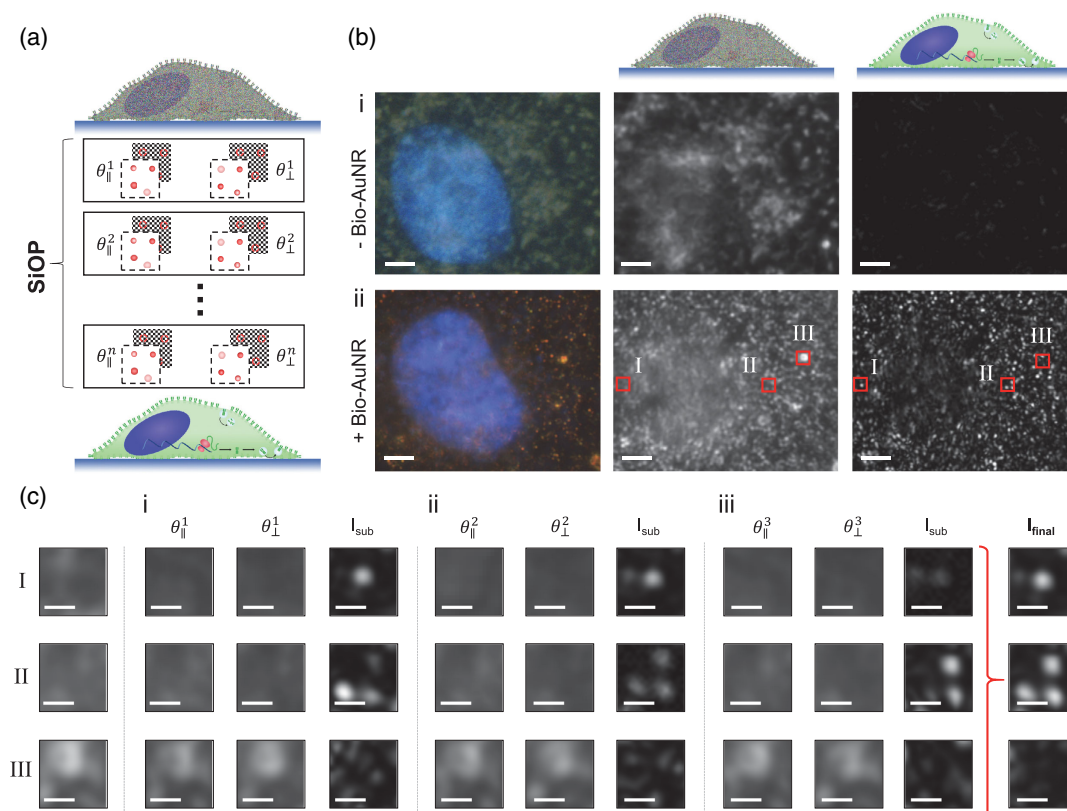


Figure 4. Nanoscopic background elimination demonstrates two orders of magnitude increase in signal-to-noise in SH-SY5Y cells. a) Conceptual schematic of nanoscale background elimination by SiOP. b) i) SH-SY5Y cells without nanoprobe: (left) color overlay of dark-field and fluorescently stained nucleus, (middle) dark-field image, (right) SiOP image. ii) SH-SY5Y cells with nanoprobe: (left) color overlay of dark-field and fluorescently stained nucleus, (middle) dark-field image, (right) SiOP image. I-III: region of interest corresponding to part c. Scale bar: 1 μ m. c) Magnified region of interest corresponding to part b. i) Representative orthogonal pair 1: region of interest I: θ_{\parallel}^1 : 30°, θ_{\perp}^1 : 120°, I_{sub} : subtracted image of orthogonal pair. Region of interest II: θ_{\parallel}^2 : 0°, θ_{\perp}^2 : 90°, I_{sub} : subtracted image of orthogonal pair. Region of interest III: θ_{\parallel}^3 : 65°, θ_{\perp}^3 : 155°, I_{sub} : subtracted image of orthogonal pair. ii) Representative orthogonal pair 2: region of interest I: θ_{\parallel}^2 : 10°, θ_{\perp}^2 : 100°, I_{sub} : subtracted image of orthogonal pair. Region of interest II: θ_{\parallel}^2 : 30°, θ_{\perp}^2 : 120°, I_{sub} : subtracted image of orthogonal pair. Region of interest III: θ_{\parallel}^2 : 55°, θ_{\perp}^2 : 145°, I_{sub} : subtracted image of orthogonal pair. iii) Representative orthogonal pair 3: Region of interest I: θ_{\parallel}^3 : 65°, θ_{\perp}^3 : 155°, I_{sub} : subtracted image of orthogonal pair. Region of interest II: θ_{\parallel}^3 : 50°, θ_{\perp}^3 : 140°, I_{sub} : subtracted image of orthogonal pair. Region of interest III: θ_{\parallel}^3 : 0°, θ_{\perp}^3 : 90°, I_{sub} : subtracted image of orthogonal pair. Finally, SiOP sums images I_{sub} over the entire polarization range to obtain the final image I_{final} . Scale bar: 200 nm.

nanoprobes, which were not visible due to background scattering. We also performed a time course analysis of the Pearson coefficient r between the first and last images within one SiOP imaging cycle as a quantitative metric for image similarity over time during bioimaging (Figure S7, Supporting Information). Time course analysis displayed r close to 1, verifying stability of our method over time. Finally, in region of interest III (Figure 4c), background artifacts were eliminated by subtracting dark-field images for orthogonal pair of polarizations over the polarization range and obtaining a final background-free image I_{final} . Using SiOP, we were able to achieve two orders of magnitude enhancement in SNR (Figure S8, Supporting Information). We also applied our method to other biological samples (Figure S9, Supporting Information). Nanoprobes were selectively bound to actin filaments. Prior to applying our method, the exact locations of nanoprobes were not distinguishable. Applying our method eliminated the protein background and significantly enhanced the SNR of the nanoprobes, enabling the exact locations of nanoprobes to be ascertained.

One benefit of our method is enhanced SNR. This method allows for clear visualization of biomolecules labeled with metallic nanoprobes without photobleaching. In addition to enhanced SNR, another benefit of our method is the ability to process orthogonal pairs at high speed. Without spatial errors such as drifting and movement artifacts, this method will allow for precise tracking of biomolecular dynamics needed for in-depth understanding of functions of biomolecules within living cells. This method will also aid long-term bioimaging and live cell imaging efforts currently hampered by drifting and movement artifacts. Recently, super-resolution imaging has allowed for overcoming the diffraction barrier to observe nanoscale spatial details. Super-resolution imaging can require hours to obtain a complete image stack of as many as $\approx 100\,000$ images, limiting real-time acquisition. This method can be used in applications of real-time super-resolution where background suppression is critical and time constraints currently limit real-time capabilities.

In conclusion, we have demonstrated high-speed nanoscopic background elimination by SiOP. By processing orthogonal pairs in real time, our method minimizes the potential for movement artifacts during the background elimination process. We showed spatial shifts result in low SNR and distortion, which significantly deteriorate background suppression. Using SiOP, we demonstrated two orders of magnitude enhancement in SNR in cellular imaging. We anticipate nanoscale background elimination that will aid the ability to accurately track biomolecules and their dynamics in living cells.

Supporting Information

Supporting Information is available from the Wiley Online Library or from the author.

Acknowledgements

This work was supported by the Air Force Office of Scientific Research (AFOSR FA9550-16-1-0272, FA9550-19-1-0186, FA9550-22-1-0285), the National Science Foundation (NSF 1454188), and academic research fund at the University of Michigan.

Conflict of Interest

The authors declare no conflict of interest.

Data Availability Statement

The data that support the findings of this study are available from the corresponding author upon reasonable request.

Keywords

background-free, bioimaging, bioplasmonics, gold nanorod, plasmonics

Received: June 28, 2022

Revised: September 26, 2022

Published online:

- [1] G. Nettesheim, I. Nabti, C. U. Murade, G. R. Jaffe, S. J. King, G. T. Shubeita, *Nat. Phys.* **2020**, *16*, 1144.
- [2] M. Fernández-Suárez, A. Y. Ting, *Nat. Rev. Mol. Cell Biol.* **2008**, *9*, 929.
- [3] E. Betzig, G. H. Patterson, R. Sougrat, O. W. Lindwasser, S. Olenych, J. S. Bonifacino, M. W. Davidson, J. Lippincott-Schwartz, H. F. Hess, *Science* **2006**, *313*, 1642.
- [4] M. J. Rust, M. Bates, X. Zhuang, *Nat. Methods* **2006**, *3*, 793.
- [5] T. Dertinger, R. Colyer, G. Iyer, S. Weiss, J. Enderlein, *Proc. Natl. Acad. Sci.* **2009**, *106*, 22287.
- [6] T. A. Klar, S. W. Hell, *Opt. Lett.* **1999**, *24*, 954.
- [7] S. W. Hell, M. Kroug, *Appl. Phys. B* **1995**, *60*, 495.
- [8] M. Hofmann, C. Eggeling, S. Jakobs, S. W. Hell, *Proc. Natl. Acad. Sci.* **2005**, *102*, 17565.
- [9] C. Sönnichsen, A. P. Alivisatos, *Nano Lett.* **2005**, *5*, 301.
- [10] P. Zijlstra, J. W. M. Chon, M. Gu, *Nature* **2009**, *459*, 410.
- [11] Y. Liu, Y. Park, S. E. Lee, *Appl. Phys. Lett.* **2016**, *109*, 013109.
- [12] E. Murphy, Y. Liu, D. Krueger, M. Prasad, S. E. Lee, Y. Park, *Small* **2021**, *17*, 2006044.
- [13] W. K. Lin, G. Cui, Z. Burns, X. Zhao, Y. Liu, Z. Zhang, Y. Wang, X. Ye, Y. Park, S. E. Lee, *Adv. Mater. Interfaces* **2021**, *8*, 2001370.
- [14] Y. Liu, Z. Zhang, Y. Park, S. E. Lee, *Small* **2021**, *17*, 2007610.
- [15] S. E. Lee, Q. Chen, R. Bhat, S. Petkiewicz, J. M. Smith, V. E. Ferry, A. L. Correia, A. P. Alivisatos, M. J. Bissell, *Nano Lett.* **2015**, *15*, 4564.
- [16] S. E. Lee, A. P. Alivisatos, M. J. Bissell, *Syst. Biomed.* **2013**, *1*, 12.
- [17] S. E. Lee, D. Y. Sasaki, Y. Park, R. Xu, J. S. Brennan, M. J. Bissell, L. P. Lee, *ACS Nano* **2012**, *6*, 7770.
- [18] S. E. Lee, L. P. Lee, *Curr. Opin. Chem. Biol.* **2010**, *14*, 623.
- [19] S. E. Lee, L. P. Lee, *Curr. Opin. Biotechnol.* **2010**, *21*, 489.
- [20] E. L. Somin, D. Y. Sasaki, T. D. Perroud, D. Yoo, K. D. Patel, L. P. Lee, *J. Am. Chem. Soc.* **2009**, *131*, 14066.
- [21] M. W. Knight, L. Liu, Y. Wang, L. Brown, S. Mukherjee, N. S. King, H. O. Everitt, P. Nordlander, N. J. Halas, *Nano Lett.* **2012**, *12*, 6000.
- [22] S. E. Lee, G. L. Liu, F. Kim, L. P. Lee, *Nano Lett.* **2009**, *9*, 562.
- [23] J. Pérez-Juste, B. Rodríguez-González, P. Mulvaney, L. M. Liz-Marzán, *Adv. Funct. Mater.* **2005**, *15*, 1065.
- [24] X. Huang, I. H. El-Sayed, W. Qian, M. A. El-Sayed, *Nano Lett.* **2007**, *7*, 1591.
- [25] G. Wang, W. Sun, Y. Luo, N. Fang, *J. Am. Chem. Soc.* **2010**, *132*, 16417.
- [26] W. S. Chang, J. W. Ha, L. S. Slaughter, S. Link, *Proc. Natl. Acad. Sci.* **2010**, *107*, 2781.

- [27] Z. Zhang, H. Jeong, D. Zu, X. Zhao, P. Senaratne, J. Filbin, B. Silber, S. Kang, A. Gladstone, M. Lau, G. Cui, Y. Park, S. E. Lee, *Nanophotonics* **2022**, *11*, 4419.
- [28] Y. Park, H. J. Yoon, S. E. Lee, L. P. Lee, *ACS Nano* **2022**, *16*, 2013.
- [29] T. Saha, J. Mondal, S. Khiste, H. Lusic, Z.-W. Hu, R. Jayabalan, K. Hodgetts, H. Jang, S. Sengupta, S. E. Lee, Y. Park, L. P. Lee, A. Goldman, *Nanophotonics* **2021**, *10*, 3063.
- [30] X. Cheng, X. Cao, B. Xiong, Y. He, E. S. Yeung, *Nano Res.* **2017**, *10*, 1423.
- [31] J. Aaron, E. de la Rosa, K. Travis, N. Harrison, J. Burt, M. José-Yacamán, K. Sokolov, *Opt. Express* **2008**, *16*, 2153.
- [32] Y. Chen, X. Chen, Q. Cao, K. Xu, *Plasmonics* **2015**, *10*, 1883.
- [33] M. Atakhorrani, K. M. Addas, C. F. Schmidt, *Rev. Sci. Instrum.* **2008**, *79*, 043103.